

Solar Photocatalytic Degradation of Rhodamine B using Co-Doped TiO₂ Nanoparticles

Bhosale RR¹, Pujari SR¹, Muley GG², Kande SR³, Ghoshir UG³, Kalokhe SB³, Gambhire AB^{3*}

¹D.B.F. Dayanad College of Arts and Science, Solapur, 413002, Maharashtra, India,

²Dept of Physics, SGB Amravati Univeristy, Amravati, 444602, Maharashtra, India,

³Dept of Chemistry, Shri Anand College, Pathardi, Ahmednagar, 414102, MS, India

E-mail: abg_chem@ymail.com

Manuscript Details

Available online on <http://www.irjse.in>
ISSN: 2322-0015

Editor: Dr. Arvind Chavhan

Cite this article as:

Bhosale RR, Pujari SR, Muley GG, Kande SR, Ghoshir UG, Kalokhe SB, Gambhire AB. Solar Photocatalytic Degradation of Rhodamine B using Co-Doped TiO₂ Nanoparticles, , *Int. Res. Journal of Science & Engineering*, January 2018, Special Issue A2 : 195-201.

© The Author(s). 2018 Open Access

This article is distributed under the terms of the Creative Commons Attribution 4.0 International License

(<http://creativecommons.org/licenses/by/4.0/>), which permits unrestricted use, distribution, and reproduction in any medium, provided you give appropriate credit to the original author(s) and the source, provide a link to the Creative Commons license, and indicate if changes were made.

ABSTRACT

A series of co-doped TiO₂ nanocomposites were synthesized by doping Fe(III), Zn(II), Zr(IV) Sb(III), Ce(IV) with C and N, separately by sol-gel method, combined with surfactant incorporation method. The as prepared sample were characterized by X-ray diffraction (XRD), Transmission electron microscopy (TEM), X-ray photoelectron spectroscopy (XPS), Brunauer-Teller method (BET), UV-Vis diffuses reflectance spectroscopy (DRS) and Photoluminescence spectroscopy (PL). The results shows that phase composition, crystallite size, BET surface area and optical absorption of co-doped TiO₂ nanocomposites varied significantly with the nature dopants. The photocatalytic activities of these co-doped TiO₂ nanocomposites were investigated by degradation Rhodamine B (RhB) in aqueous solution under solar-light illumination. The results showed an appreciable enhancement in the photoactivity of the Fe, C co-doped TiO₂ (Fe-C/TiO₂) as compared to other co-doped TiO₂ because of smaller particle size, higher surface area and the synergistic effect created by higher solar-light absorption and the improved charge separation. The degradation rate of Rhodamine B (RhB) reached 99% in 30 min which is about 10 times higher than that of pure TiO₂ photocatalyst.

Keywords: Co-dopant, Sol-gel process, Nanomaterials, Photocatalytic activity.

INTRODUCTION

Heterogeneous photocatalysis has received a great deal of attention as an advanced oxidation process for the treatment of air and water streams [1-3]. Among the various semiconductors studied, TiO₂ is the most promising and extensively studied photocatalyst because of the biological and chemical inertness, high stability and strong oxidizing power [4, 5]. However, high photocatalytic activities of photocatalyst are primarily determined by its physicochemical properties such as crystallite structure, particles size, specific surface area and the use of renewable solar energy. Doping of TiO₂ with transition metals and non-metals was reported in the literature [6]. It came to light that C-doped TiO₂ showed an appreciable enhancement in the photocatalytic activity under solar-light illumination. In addition, composites, such as co-doped TiO₂ with *3d* transition metals (such as Mo, W and Os) and nonmetals (such as C, N, F) can reduce recombination of separated electron-hole pairs and enhance the photocatalytic activity [7, 8] as a result of a synergistic effect among co-dopants [9]. Gai et al., showed that co-doping of TiO₂ with Mo and C significantly enhance water splitting capability of composite material [10]. Further, Cu-N [11], N-F [12], Mo-N [13], W-N [14] and Fe-N, Ni-N, Ag-N, Pt-N co-doped TiO₂ [15], were also investigated to improve the photocatalytic activity. The doping of two kinds of atoms into TiO₂ has gained much attention because it resulted in higher photocatalytic activity than single element doping. This effect could be due to the synergistic effect of the doped two kinds of atoms [16]. This synergistic effect of the combination of transition metals with carbon and nitrogen on TiO₂ has previously reported for the degradation of some organic molecules in the photocatalytic process [9, 11]. The enhanced photocatalytic activity obtained with co-doping of TiO₂ with metals and non-metals might be due to common contact interface between the different solid phases in TiO₂ and synergistic effect created by the higher visible light absorption and the improved charge separation capability.

Although, there are many merits for co-doped TiO₂ with metals and non-metals, few studies have been reporting the comparative study on photocatalytic degradation of organic compound using a series of

transition metals and non-metals co-doped TiO₂. In the present study, a series of co-doped TiO₂ nanocomposites were synthesized by doping transition metals with carbon and nitrogen, separately towards photocatalytic decomposition of RhB. Furthermore, most of the research work has been carried out by irradiating catalyst suspension with artificial visible light [13-16], which is not feasible and economical. The present study focuses on the efficient use of sunlight and the ability of prepared photocatalyst to decompose RhB under solar light illumination using a series of co-doped TiO₂ nanocomposites synthesized by sol-gel method.

METHODOLOGY

2.1 Synthesis of co-doped TiO₂:

The dopants starting materials; metal nitrates of Fe(III), Zn(II), Zr(IV), Sb(III), Ce(IV)-loaded (3 wt.%) TiO₂ nanomaterials were synthesized by sol-gel process. Titanium butoxide (98%, Aldrich) was used as the precursor of TiO₂. An amount, 25 ml of titanium butoxide was hydrolyzed in 300 ml water containing 1.5 ml nitric acid. The cationic surfactant cetyltrimethylammonium bromide (CTAB), 20% (10 ml) in ethanol was dropped into the above solution. Gel formed was stirred continuously at room temperature to form a highly dispersed sol. To this, Fe, Zn, Zr, Sb, and Ce (3 wt.%) solutions were added, separately to synthesize metal ion containing TiO₂ sol. Then, a certain amounts of ethylene glycol and citric acid (source of carbon) in 50 ml of deionized water were added drop wise into this sol under vigorous stirring. The resulted alkoxide solution was left hydrolyzing to the TiO₂ sol. After keeping the sol for aging (5 days), it was concentrated and dried at 80°C. The samples, after overnight drying at 110°C, were calcined for 2 h at 500°C. Meanwhile, in the second set of samples, a certain amount of ammonia (source of nitrogen) in 50 ml deionized water were added drop-wise to the solution of above mentioned metal nitrate-TiO₂ sol, separately in order to synthesize metal-nitrogen co-doped TiO₂. The remaining process is similar as per the above used to synthesize metal-carbon co-doped TiO₂.

2.2 Characterization:

X-ray powder diffraction (XRD) patterns have been recorded on a model D8 Bruker AXS with monochromatic Cu radiation (40 kV and 30 mA), over the 2θ collection range of 20-80°. The particle size of anatase was calculated from XRD measurement. BET surface area measurements were carried out using a Quantachrome NOVA 1200 instrument. The microscopic nanostructures were observed by transmission electron microscopy (TEM; FEI, Tecnai F30, HRTEM, FEG operated at 300 kV). FT-IR spectra were recorded on a Shimadzu-8400 spectrometer in the range of 4000-500 cm^{-1} . X-ray photoelectron spectroscopy (XPS; ESCA-3000, VG Microtech, Uckfield, UK) was used to study the chemical composition of the samples. Non-chromatic X-ray beams of Al $K\alpha$ ($h\nu = 1486.6$ eV) and Mg $K\alpha$ ($h\nu = 1253.6$ eV) radiation were used as the excitation source. A hemispherical sector analyzer and multichannel detectors were used to detect the ejected photoelectrons as a function of their kinetic energies. XPS spectra were recorded at a pass-energy of 50 eV, 5-mm slit width and a take-off angle of 55°. The spectrometer was calibrated by determining the binding energy values of the Au4f_{7/4} (84.0 eV), Ag3d_{5/2} (368.4 eV) and Cu2P_{3/2} (932.6 eV) levels using spectroscopically pure materials. The instrumental resolution under these conditions was 1.6 eV full-width at half-maximum (FWHM) for Au4f_{7/4} level. The Cls (285 eV) and Au 4f_{7/4} (84.0 eV) were used as internal standards when needed. Photoluminescence (PL) spectra measured at room temperature on a fluorescence spectrophotometer (F-7000, Hitachi, Japan) with an excitation wavelength of 315 nm, scan rate of 1200 nm/min and PMT voltage of 700 V. The excitation and emission slits both had a width of 5.0 nm. FT-IR spectra were recorded on a Shimadzu-8400 spectrometer in the range of 4000-500 cm^{-1} . UV-Vis diffuse reflectance spectra (UV-Vis-DRS) were recorded in an air at room temperature in the wavelength range of 200-800 nm using a PE LAMBDA35 spectrophotometer.

2.3 Photocatalytic activity:

All the solar photocatalytic experiments were carried out at the same conditions on March 2017 from 12.00 p.m. to 1.00 p.m. Solar light was used as the irradiation source, and the average insolation of the

solar irradiation was 25.28 W/m^2 measured by an UV irradiance meter at range of 375-475 nm. Photocatalytic experiments were carried out by adding 10 mg of photocatalyst to 50 ml of aqueous RhB (50 ppm) solution. Prior to irradiation, the suspensions were magnetically stirred in the dark for 30 min to ensure establishment of an adsorption-desorption equilibrium among the photocatalyst, RhB and atmospheric oxygen. At a given irradiation time interval, 10 ml of the suspension was collected, and then filtered through a Millipore filter to separate the photocatalyst. The changes in RhB concentration were analyzed by a UV-Visible spectrophotometer and the absorption peak at 650 nm was recorded.

RESULTS AND DISCUSSION

3.1. XRD analysis:

To understand phase symmetry in the calcined samples, a systematic X-ray diffraction study was undertaken. Fig. 1 (a-k) shows the XRD patterns of the pure TiO_2 , and co-doped TiO_2 with transition metal, N and S, separately.

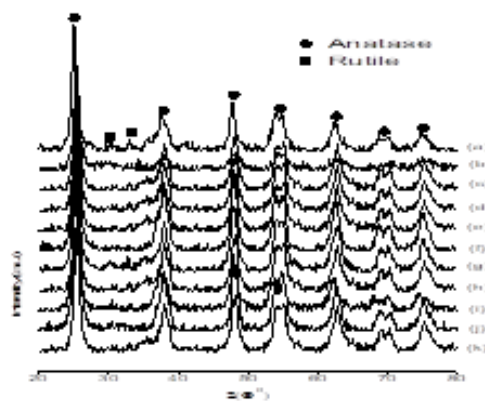


Fig. 1(a-k). XRD profiles of (a) Pure TiO_2 , (b) Fe-C/ TiO_2 , (c) Fe-N/ TiO_2 , (d) Zn-C/ TiO_2 , (e) Zn-N/ TiO_2 , (f) Zr-C/ TiO_2 , (g) Zr-N/ TiO_2 , (h) Sb-C/ TiO_2 , (i) Sb-N/ TiO_2 , (j) Ce-C/ TiO_2 , (k) Ce-N/ TiO_2 .

Pure TiO_2 shows two main peaks at $2\theta = 25.4$ and 27.5 , corresponding to (101) phase of anatase and (110) phase of rutile, respectively. In the case of co-doped TiO_2 , the rutile phase is $< 1\%$, which means co-doping retards the transformation from anatase to rutile phase. Co-doping of the TiO_2 stabilizes a well-crystallized pure anatase upon calcination at 500°C , in

contrast with the simultaneous growth of the rutile phase observed for the pure TiO_2 . Further, all peaks measured by XRD analysis could be assigned to those of TiO_2 crystal. No peaks corresponding to the metal and non-metal oxide is detected. The peaks of TiO_2 have been slightly shifted due to solid solution of metal and non-metal ion with TiO_2 . The average particle sizes of the samples were calculated using Debye-Scherrer formula based on the XRD peak broadening analysis at 101 peaks, listed in Table 1. The particle size calculated from XRD data is as large as 15-20 nm for the Zr-C/ TiO_2 , Zr-N/ TiO_2 , Sb-C/ TiO_2 , Sb-N/ TiO_2 , Ce-C/ TiO_2 , Ce-N/ TiO_2 and as small as 7-10 nm for the Fe-C/ TiO_2 , Fe-N/ TiO_2 , Zn-C/ TiO_2 , Zn-N/ TiO_2 . This apparent fall in the particle size (higher specific surface area) will ensure higher photocatalytic activity for the Fe-C/ TiO_2 , Fe-N/ TiO_2 ,

Zn-C/ TiO_2 , and Zn-N/ TiO_2 , when it is used for photocatalytic applications.

3.2. TEM analysis:

In order to confirm the effect co-doping on particle size of TiO_2 and hence higher specific surface area, the particle size of Fe-C/ TiO_2 , Fe-N/ TiO_2 , Zn-C/ TiO_2 , and Zn-N/ TiO_2 samples were observed using TEM. Fig. 2(a-d) shows TEM images of (a) Fe-C/ TiO_2 , (b) Fe-N/ TiO_2 , (c) Zn-C/ TiO_2 , and (d) Zn-N/ TiO_2 samples and its corresponding Fourier transfer patterns (FTT) are also presented in the inset of figures. It can be seen that the particle size of Fe-C/ TiO_2 , and other co-doped samples (Fe-N/ TiO_2 , Zn-C/ TiO_2 , Zn-N/ TiO_2) are about 7 and 10 nm, respectively.

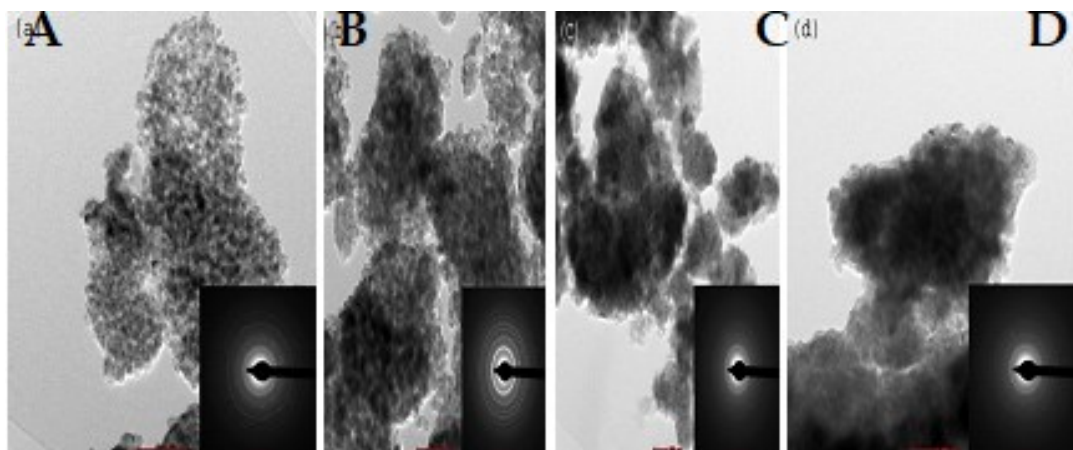


Fig. 2(a-d). Typical TEM images of (a) Fe-C/ TiO_2 , (b) Fe-N/ TiO_2 , (c) Zn-C/ TiO_2 , and (d) Zn-N/ TiO_2 ; and the inset of Fig. 2(a-d) are its corresponding FFT.

Table 1: Characteristics of co-doped TiO_2 composites after heat treatment for 2 h at 500°C.

Samples	Average crystalline size (nm)		BET [m^2/g]	Energy of the band gap (eV)
Pure TiO_2	22.50	30	3.2	30.40
Fe-C/ TiO_2	7.00	146	2.25	99.00
Fe-N/ TiO_2	10.37	133	2.63	90.00
Zn-C/ TiO_2	10.00	140	2.75	86.56
Zn-N/ TiO_2	10.65	104	2.77	84.00
Zr-C/ TiO_2	16.32	82	2.72	57.80
Zr-N/ TiO_2	18.00	65	2.82	53.48
Sb-C/ TiO_2	20.22	60	2.30	64.00
Sb-N/ TiO_2	19.00	65	2.30	62.20
Ce-C/ TiO_2	15.21	100	2.90	65.00
Ce-N/ TiO_2	15.01	103	2.77	65.00

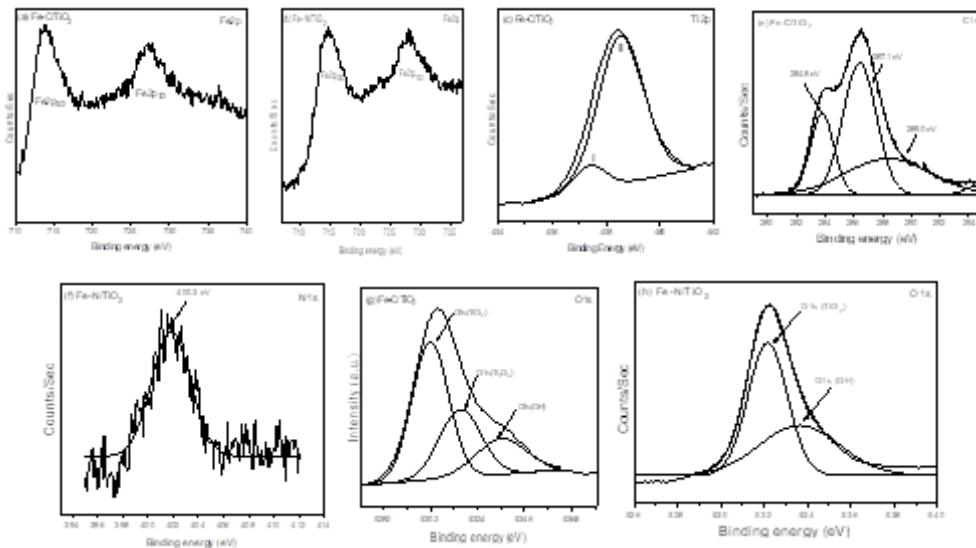


Fig. 3(a-h). High resolution XPS spectra of the Fe2p, Ti2p, C1s, N1s, O1s taken on Fe-C/TiO₂ and Fe-N/TiO₂.

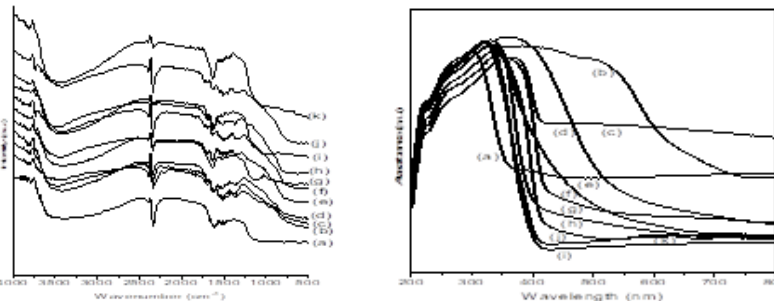


Fig. 4(a-k). F-IR spectra of (a) pure TiO₂, (b) Fe-C/TiO₂, (c) Fe-N/TiO₂, (d) Zn-C/TiO₂, (e) Zn-N/TiO₂, (f) Zr-C/TiO₂, (g) Zr-N/TiO₂, (h) Sb-C/TiO₂, (i) Sb-N/TiO₂, (j) Ce-C/TiO₂, (k) Ce-N/TiO₂.

Fig. 5(a-k). UV-Vis-DR spectra of (a) pure TiO₂, (b) Fe-C/TiO₂, (c) Fe-N/TiO₂, (d) Zn-C/TiO₂, (e) Zn-N/TiO₂, (f) Zr-C/TiO₂, (g) Zr-N/TiO₂, (h) Sb-C/TiO₂, (i) Sb-N/TiO₂, (j) Ce-C/TiO₂, (k) Ce-N/TiO₂.

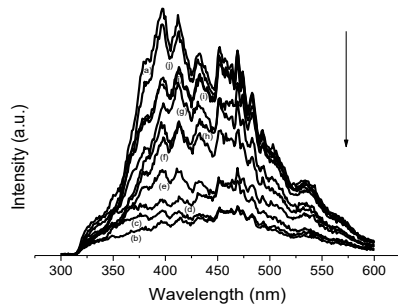


Fig. 6(a-k). PL spectra of (a) pure TiO₂, (b) Fe-C/TiO₂, (c) Fe-N/TiO₂, (d) Zn-C/TiO₂, (e) Zn-N/TiO₂, (f) Zr-C/TiO₂, (g) Zr-N/TiO₂, (h) Sb-C/TiO₂, (i) Sb-N/TiO₂, (j) Ce-C/TiO₂, (k) Ce-N/TiO₂.

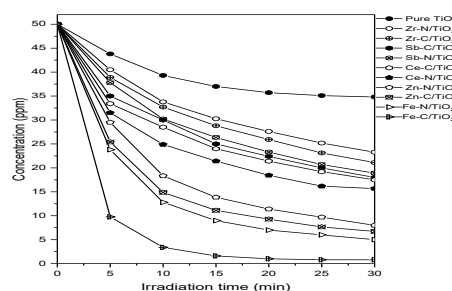


Fig. 7(a-k). Rate of decomposition of RhB by using (a) pure TiO₂, (b) Fe-C/TiO₂, (c) Fe-N/TiO₂, (d) Zn-C/TiO₂, (e) Zn-N/TiO₂, (f) Zr-C/TiO₂, (g) Zr-N/TiO₂, (h) Sb-C/TiO₂, (i) Sb-N/TiO₂, (j) Ce-C/TiO₂, (k) Ce-N/TiO₂.

3.3. BET surface area:

All co-doped samples exhibit relatively high specific surface areas with respect to pure TiO₂ (Table 1). Co-doping reduces the extent of surface area loss during high temperature calcinations. This is based on higher resistance to sintering as well as the delayed transformation from amorphous to crystalline state

acquired by co-doping with metal and non-metal. The metal oxide species, along with the non-metal ions, prevent the agglomeration of TiO₂ particles, resulting in a higher specific surface area. The surface area of Fe-C/TiO₂, Fe-N/TiO₂, Zn-C/TiO₂, and Zn-N/TiO₂ samples are 146, 133, 140, and 121 m²g⁻¹, respectively.

3.4. XPS studies:

The spectra of Fe2p, Ti2p, C1s, N1s and O1s level were recorded under the same conditions of vacuum and pass energy. Fig. 3(a-b) shows high resolution XPS spectra of Fe2p region of Fe-C/TiO₂ and Fe-N/TiO₂, respectively. The Fe2p spectra of both samples shows peak positions at binding energies of 710.8 eV which correspond to elements in the oxidation states Fe³⁺. The Ti2p_{3/2} level of Fe-C/TiO₂ (Fig.3(c)) shows asymmetry towards the lower binding energy side. The peaks resolved into two components, with binding energy values of 457.5 and 458.6 eV for the first and second components, respectively. These binding energies are well matching with the binding energy value of Ti₂O₃ and TiO₂ [17].

On the contrary Fe-N/TiO₂ sample (Fig. 3(d)) shows two peaks centered at 458.4 eV and 464.1 eV assigned to Ti2p_{3/2} and Ti2p_{1/2} states of Ti⁴⁺. The formation of Ti₂O₃ (Ti³⁺) in Fe-C/TiO₂ sample might be due to the reduction carbon in the layer at 500°C draws oxygen from the surrounding atmosphere, which causes a reduction of some Ti(IV) to Ti(III) species. The C1s spectra of Fe-C/TiO₂ sample (Fig. 3(e)) shows C-C and C-H at 284.8 eV, residual oxygenated moieties at 287.1 eV and C-O bonds at 289.0 eV. The N1s XPS spectra of Fe-N/TiO₂ sample (Fig. 3(f)) shows peak at around 400.3 eV indicating the presence of N-containing species [13]. The O1s level of Fe-C/TiO₂ (Fig. 3(g)) shows broadening and asymmetry towards the higher binding energy side. These peaks are also resolved into three components with binding energies values of 530.5, 531.7, 533.4 eV for the first, second and third peak, respectively. The binding energy of the first, second and third peak is well matching with the binding energy of TiO₂ and Ti₂O₃ lattice oxygen, respectively, while the third peak is either adsorbed oxygen or hydroxyl species on the surface. The O1s spectra of Fe-N/TiO₂ (Fig. 3 (h)) shows two peaks centered at 530.4 eV and 533.5 eV, assigned to TiO₂ lattice oxygen, while the second peak is either adsorbed oxygen or hydroxyl species on the surface.

3.5. FT-IR analysis:

Fig. 4(a-k) shows FT-IR spectra of samples in the range of 4000 to 500 cm⁻¹. Within this it shows up the band corresponding to surface hydroxyl groups. Two

clear bands can be seen Fig. 4(a-k), one around 3400 cm⁻¹ and a second one located around 3185 cm⁻¹. These bands can be attributed to the different OH groups at the surface, in which one is ascribed to adsorbed water and the other is surface hydroxyl group of TiO₂ [18]. The bands in the low-wave number region (400-600 cm⁻¹) can be assigned to Ti-O bond vibrations [19]. The FT-IR spectra of the modified samples do not show any band corresponding to the transition metal oxide, which confirms the XRD results.

3.6. UV-vis DR spectral analysis:

UV-vis diffuse reflectance spectroscopy Fig. 5(a-k) permits the detection of frame work of Ti in the samples. In all the samples, characteristic band for tetrahedrally coordinated titanium appears at about 350 nm. A progressive red-shift in the band gap absorption is noticed with co-doping than that pure TiO₂. The edges of the absorption of the metal incorporated samples were shifted to approximately 500 nm, corresponding to band gap energy of 2.25 eV. The absorption is associated to the O²⁻ → Ti⁴⁺ charge-transfer, corresponding to electronic excitation from the valence band to the conduction band. The absorption onsets were determined by linear extrapolation from the inflection point of the curve to the baseline.

3.7. Photoluminescence study:

In PL process, an electron is excited from valence to conduction band by monochromatic light having photon energy equal to greater than band gap. The radiative recombination of an excited electron either takes place at the edge of valence band or through traps within the band gap. The lower PL intensity may indicate the lower radiative recombination rate of electrons and holes. As shown in Fig. 6(a-k) their PL intensities decreases in the order of TiO₂>Ce-C/TiO₂>Sb-N/TiO₂>Zr-N/TiO₂>Sb-C/TiO₂>Zr-C/TiO₂>Zn-N/TiO₂>Zn-C/TiO₂>Fe-N/TiO₂>Fe-C/TiO₂. C and N-doping suppresses the photogenerated charge separation, which should be due to the mid-gap states introduced by C and N-doping as recombination centers [20]. Conventionally, the higher the recombination rate is, the stronger the PL peak intensity is [21].

3.8. Photocatalytic activity:

The photocatalytic activities of pure TiO₂ and co-doped TiO₂ are shown in Fig. 7(a-k). In the presence of pure TiO₂ decomposition of RhB was not observed. However, in the presence of co-doped TiO₂, the decomposition of RhB obviously increased. Among the different co-doped samples, Fe-C/TiO₂ exhibited the highest photocatalytic activity under solar light irradiation, only 1% of RhB remained, and in the case of Fe-N/TiO₂, Zn-C/TiO₂, Zn-N/TiO₂ 10-15% of RhB remained after exposure to solar light for 30 min. While as high as 40-50% remained in the case of Zr-C/TiO₂, Zr-N/TiO₂, Sb-C/TiO₂, Sb-N/TiO₂, Ce-C/TiO₂, and Ce-N/TiO₂. These results are in good agreement with previously reported work, excluding the time needed for the decomposition of organic dye was double using C-TiO₂ [6], in comparison with the present work. From the observed results it was found that the Fe-C/TiO₂ is found to be composite photocatalyst, once optical excitation occurs, the photogenerated electrons can transferred to the lower-lying conduction bands of Fe-C, while the holes will accumulate in the valence band of TiO₂, and effectively scavenged by the photo-oxidation of RhB, whereas the photogenerated electrons can be transferred into the surface of Fe-C, rather than undergoing bulk recombination. The PL spectra of Fe-C/TiO₂ show weaker peak intensity indicates enhancement in the efficiency of photo-excited charges separation. The enhancement may be explained in terms of the synergistic effect on the specific adsorption property and efficient photo-excited charges separation at the Fe-C/TiO₂ nanocomposite photocatalyst. Further, the high surface area of Fe-C/TiO₂ effectively concentrates RhB around it and produces high concentrations of organic compounds for the TiO₂ photocatalyst. Furthermore, the carbon in Fe-C/TiO₂ reduces TiO₂ to form Ti³⁺ ions. Ti³⁺ can trap photogenerated electron in the conduction band and prevent the recombination of photo-excited charges under solar-light irradiation. Thus, increase in Ti³⁺ content enhances photocatalytic activity [22], which is evident from XPS spectra showing the formation of Ti³⁺ species. Moreover, co-doped samples shows red-shift in the absorption range compared with pure TiO₂. The existence of oxygen deficiencies, leads to localized electronic states

between the valence and conduction band, shows certain absorption in the visible range.

CONCLUSION

Co-doped TiO₂ nanoparticles were successfully prepared by sol-gel method. The prepared samples were characterized by XRD, TEM, FT-IR, XPS, PL and UV-Vis-DRS techniques. It was found that the prepared photocatalyst exhibited smaller shape particles and higher specific surface area. In addition to oxides of Ti⁴⁺, there was a certain amount of Ti³⁺ oxides existed in Fe-C/TiO₂ photocatalyst. The Fe-C/TiO₂ photocatalyst shows superior photocatalytic activity than other co-doped samples. The highest photocatalytic activity of the composite catalyst could be attributed to the synergistic effects of enhanced solar-light absorption, efficient charge separation.

Acknowledgement: This work was financed by Science & Engineering Research Board (SERB), New Delhi, India, Grant No. SB/EMEQ-029/2014.

Conflicts of interest: The authors stated that no conflicts of interest.

REFERENCES

1. Molinari A, Sarti E, Marchetti N, Pasti L, *Appl. Catal. B: Environ.* 2017; 203, 9-17.
2. Garza-Campos BR, Guzmán-Mar JL, Reyes LH, Brillas E, Hernández-Ramírez A, Ruiz-Ruiz EJ, *Chemosphere*, 2014; 97, 26-33.
3. Parent Y, Blake D, Magrini-Bair K, Lyons C, Turchi C, Watt A, Wolfrum E, Prairie M, *Solar Energy*, 1996; 56, 429-437.
4. Gambhire AB, Lande MK, Arbad BR, Rathod SB, Gholap RS, Patil KR, *Mater. Chem. Phys.*, 2011; 125: 807-812.
5. Momeni M, Saghafian H, Golestani-Fard F, Barati N, Khanahmadi A. *Appl. Surf. Science*, 2017; 392 : 80-87.
6. Bhosale RR, Pujari SR, Muley GG, Patil SH, Patil KR, Shaikh MF, Gambhire AB. *Solar Energy*; 2014; 103: 473-479.
7. Gai YQ, Li JB, Li SS, Xia JB, Wei SH. *Phys. Rev. Lett.*, 102 (2009) 036402.